Arabian Journal of Chemistry (2021) **14**, 102961

King Saud University

Arabian Journal of Chemistry

www.ksu.edu.sa
www.sciencedirect.com

ORIGINAL ARTICLE

A study of the anti-corrosive effects of essential oils of rosemary and myrtle for copper corrosion in chloride media

Ines Dhouibi [a], **Fatma Masmoudi** [a], **Mohamed Bouaziz** [a,b], **Mohamed Masmoudi** [a,c,*]

[a] *Laboratory of Electrochemistry and Environment (LEE), Sfax National Engineering School (ENIS) BPW, 3038 Sfax, University of Sfax, Tunisia*
[b] *Higher Institute of Biotechnology of Sfax, BP 1175, 3038, University of Sfax, Tunisia*
[c] *Preparatory Institute for Engineering Studies of Sfax, BP 805, 3018, University of Sfax, Tunisia*

Received 11 September 2020; accepted 15 December 2020
Available online 24 December 2020

KEYWORDS

Corrosion;
Myrtle;
Rosemary;
Potentiodynamic polarization;
EIS

Abstract The objective of this research work is the study of the essential oils (EOs) of myrtle (MEO) and rosemary (REO) as novel and eco-friendly corrosion inhibitors. These EOs were extracted by the Clevenger technique and analyzed using the Gas Chromatography/Mass Spectrometry (GC/MS) and Fourier-transform infrared spectroscopy (FTIR). These techniques show that MEO and REO were rich in various volatile compounds.

The investigation of copper corrosion behavior in 3 wt% NaCl solution, in the presence of EOs, via open circuit potential (OCP), potentiodynamic polarization and electrochemical impedance spectroscopy (EIS) was carried out. The results of the electrochemical tests presented the same trends: EOs acting as cathodic type inhibitor for copper in 3 wt% NaCl solutions, the inhibition efficiency increasing upon the addition of EOs and the further increase with the increase of the EOs concentration and REO having moderately superior performance compared to MEO. The EOs molecules adsorption on the copper surface followed a Langmuir isotherm, and physical adsorption (vs. chemical adsorption) is dominant.
© 2020 Published by Elsevier B.V. on behalf of King Saud University. This is an open access article under the CC BY-NC-ND license (http://creativecommons.org/licenses/by-nc-nd/4.0/).

1. Introduction

In many countries, copper and its alloys are the most prevalent materials for sea water systems. Indeed, the annual world production of copper water tubing is 500,000 tones, equivalent to 1.25 billion m or 0.75 million miles. The reasons behind this tremendous copper plumbing tube consumption are numerous, namely its ease of fabrication during installation, and hence low-installation costs, its excellent corrosion resistance as well

* Corresponding author at: Preparatory Institute for Engineering Studies of Sfax, BP 805, 3018, University of Sfax, Tunisia.
E-mail address: med_mmasmoudi@yahoo.fr (M. Masmoudi).
Peer review under responsibility of King Saud University.

ELSEVIER Production and hosting by Elsevier

https://doi.org/10.1016/j.arabjc.2020.102961
1878-5352 © 2020 Published by Elsevier B.V. on behalf of King Saud University.
This is an open access article under the CC BY-NC-ND license (http://creativecommons.org/licenses/by-nc-nd/4.0/).

as its contribution to health and the maintenance of healthy water. Moreover, copper is seen as environmentally friendly due to its potential to be 100% recycled (Zhang et al., 2019). Given the almost universal presence of water in the earth, the damage caused by aqueous corrosion affects virtually every area of human activity, from the building to the most sophisticated installations and devices such as nuclear power plants and electronic circuits, through chemical plants, oil installations and materials in contact with seawater (Nik et al., 2010).

Nevertheless, since the high concentration of Cl^- in seawater causes serious copper corrosion, it is deemed essential to protect the material against corrosion. That is why several methods for protecting metals exist, among which corrosion inhibitors are the most used ones. Actually, the most effective ones are the organic compounds. However, most of them are not eco-friendly, while being toxic and expensive. Research on green chemical compounds as a corrosion inhibition have been progressed in recent years. Inhibitors in this class are the ones that are environmentally friendly and are obtained from natural products such as plant extracts (Ahmed and Zhang, 2019; Ammouchi et al., 2019; Benarioua et al., 2019; Emembolu and Onukwuli, 2019; Fang et al., 2019; Jmiai et al., 2018; Loto and Akinyele, 2020; Popoola, 2019; Rahal et al., 2016, Refait et al., 2020), purified compounds (Kaco et al., 2018; Oyewole et al., 2020) and essential oils (Bozorg et al., 2014; Chraka et al., 2020; Cristofari et al., 2011; Idouhli et al., 2018; Mzioud et al., 2020; Rekkab et al., 2012; Znini et al., 2012). Among the widely used green inhibitors, we have selected for study, the essential oils of Myrtle (MEO) and Rosemary (REO). These two essential oils are nontoxic innocuous in the environment, biodegradable, renewable and easily extracted by a simple process (Aleksic and Knezevic, 2014; Bouzabata et al., 2015; González-Minero et al., 2020).

In Tunisia, Rosemary grows abundantly in the center and north-west of the country and Myrtle cultivates wild mainly in the coastal area, the internal hills and the forest areas in the north. These two plants grow in the domestic gardens. The use of Myrtle and Rosemary essential oils has been known since antiquity by ancient civilizations to cure common pathologies (Hennia et al., 2019; Pereira et al., 2017). Today, these essential oils are products with high added value. Thanks to its great interest in various field, such as pharmaceutical, therapeutic and industrial much research has been reported on the composition of MEO and REO (Pino et al., 1998; Elamrani et al., 2000; Perez-Alonso et al., 1995; Jamshidi et al., 2009; Bekkara et al., 2007; Zaouali et al., 2005; Asllani, 2000; Jerkovic et al., 2002; Koukos et al., 2001; Messaoud et al., 2005; Özek et al., 2000; Tuberoso et al., 2006). Nevertheless, a few studies were recently achieved to examine the effect of these two essential oils on the corrosion of various metals, including copper, in different corrosion media (Bozorg et al., 2014; Houbairi et al., 2015).

In the present paper, Myrtle and Rosemary were extracted by the Clevenger technique and the organic species present in these oils were characterized by Gas Chromatography/Mass Spectrometry (GC/MS) and Fourier-transform infrared spectroscopy (FTIR). The main objective of this work is to study the inhibiting effect of MEO and REO oils on the copper corrosion in aerated 3 wt% NaCl solution. For this reason, several electrochemical technics were used: open circuit potential (OCP), potentiodynamic polarization on a wide range of potential and voltammetry around OCP. The obtained results with electrochemical impedance spectroscopy (EIS) were compared to those given by voltammetry.

2. Experimental

2.1. Essential oils (EOs) extraction

For each plant, 1 Kg of fresh aerial parts of plant were utilized for oil extraction by steam distillation during 4 h by means of a Clevenger-type apparatus (Bouaziz et al., 2009).

After extraction, EOs were recovered directly from above the distillate without adding any solvent and stored in hermetically closed opaque-glass flasks in a refrigerator at a temperature of 4 °C, to preserve them from air, light and temperature variations, for future analysis.

The calculation of the dry weight of samples was conducted according to the moisture content that was previously determined. It was used to identify the yield of EOs as follows:

$$\text{EO Yield} = \frac{\text{Weight of the collected oil}}{\text{Dry weight of sample}} \times 100\%$$

2.2. Volatile compounds analyses

The volatile compounds were analyzed using a HP-5890 series II instrument Palo Alto, CA according to Flamini et al. (Cheraif et al., 2020). The determination of the components was carried out by comparing their retention time with that of pure authentic standards and using their linear retention indices (LRI) according to the n-hydrocarbons series. With respect to the GC–MS, they were analyzed using a Varian CP 3800 gas-chromatograph Palo Alto, CA. The constituents were determined firstly on the basis of the comparison of the retention time with that of the authentic samples. Secondly, their determination was based on the comparison of their LRI relative to the n-alkanes series, and thirdly on computer matching against commercial one (NIST 98 and ADAMS) and home-made library mass spectra built from pure substances and the components of known oils and MS literature data. Furthermore, the molecular weights of all the determined substances were affirmed by GC–MS, using MeOH as CI ionizing gas.

2.3. Fourier-transform infrared spectroscopy (FTIR)

FT-IR spectra of samples were obtained by a Perkin Elmer spectrometer. Each sample was scanned at wave number range of 4000–400 cm^{-1} with a resolution of 2 cm^{-1} for each spectrum (Hedayati et al., 2020).

2.4. Electrochemical measurements

For electrochemical studies, we made use of copper sample of purity 99.95%. The copper electrodes were masked by epoxy resin, leaving 100 mm^2 as the working surface. Before each test, the exposed surface of copper was polished by SiC paper (from grade 240 to grade1200) and rinsed with distilled water. The inhibitor solution was prepared by dissolving a mass of oil in tween 80 (m, 1/2m) to finally obtain the following concentrations: 1.25, 2.5, 5 and 10 g/L. Then, the corrosion solution was made using the prepared concentrations of essential oil as inhibitors in a 3% by weight NaCl solution. The latter was made using analytical grade sodium chloride in distilled water, treated as a blank for comparison. For each measurement, a freshly prepared solution was used. The experiments were conducted under non-stirred and naturally aerated conditions.

Corrosion inhibition ability of oils was tested in 3 wt% NaCl solution using electrochemical measurements. During the experiments, the test solutions were opened to the atmosphere, and the experiments were realized under the static conditions at 25 ± 2 °C. The electrochemical measurements were taken using an electronic potentiostat galvanostat radiometer controlled using the Volta Lab software. While, the electrochemical analyses were conducted under computer control. For all tests, the electrochemical experiments were carried out using a standard three-electrode cell configuration. A saturated calomel electrode (SCE) was utilized as the reference electrode and a platinum sheet was used as counter electrode. All potential values given in this research work were referred to on the SCE electrode.

Potentiodynamic polarization curves were plotted from −400 to 400 mV/SCE at a polarization scan rate of 0.5 mV/second. Before all experiments, the potential was stabilized at free potential during 30 min.

The voltammetry around OCP involves a larger range, for instance ± 50 mV as in this study but supposed to be adequately small to have a trivial impact on the metal/electrolyte interface. The aim is to obtain information on the kinetics of the anodic and cathodic processes occurring at OCP. However, one of the two processes can be neglected relatively to the other near OCP. Therefore, no linear part could be observed on the log | j | vs. E curve acquired around OCP even if both reactions should obey Tafel's law. That is why, it is prerequisite to have a fitting procedure of the experimental polarization curve based on electrochemical kinetic laws. The major benefit of the Tafel method that is commonly used on polarization curves obtained on a larger potential range is that different kinetic laws are likely to be used, especially for the cathodic reaction (typically O_2 reduction).

The EIS measurements were conducted after stabilization for 30 min at OCP by a sinusoidal signal with amplitude of 10 mV over a frequency range of 100 kHz to 0.1 Hz (Beikmohammadi et al., 2018; Chaudhari and Patil, 2011). The linearity of the system was verified in diversifying the signal amplitude applied to the sample. The fitting of the impedance spectra was realized using electrical equivalent circuits with EC-Lab software (Bio-Logic).

Each experiment was carried out at least in triplicate and the values given for the various determined parameters are the average of the various measurements.

3. Results and discussion

3.1. Extraction and essential oils composition

The yield acquired from the EO of the Rosemary plant is 0.91%, which is a comparable to that given by Hcini et al. for Tunisian rosemary (Hcini et al., 2013). However, the EO of the Myrtle plant has the lowest yield (0.75%). It is obvious that there are differences in the EO yields, which is acceptable since the yield depends on several biotics, such as the harvest period, the type of organs harvested, soil and rainfall.

The oils obtained from their aerial parts of Rosemary and Myrtle were colorless with a strong fragrant odor. The analysis of the oils, whose compositions are shown in Table 1, were realized by GC/MS. Forty-three compounds were separated and their structures were determined by MS and retention index data (Bouaziz et al., 2009). Our results revealed that the whole aerial parts of both plants contained different oils and compositional profiles to compare their percentages and their retention indices with those of our own authentic compound.

The EOs' chemical composition was strongly dominated by oxygenated monoterpenes, especially 1, 8-cineole and camphor. Another plentiful chemical group was the monoterpenes hydrocarbons in which α-pinene is the major compound (Fig. 1).

Monoterpene hydrocarbons were found in a low percentage in the Rosemary oil (26.9%) and in a high percentage in the Myrtle oil (49.5%). α-pinene was found to be the major monoterpene hydrocarbon in Myrtle oil (40.4%) and Rosemary oil (11.6%). Nonetheless, oxygenated monoterpenes were found in a high percentage in the Rosemary and Myrtle essential oils (59.5% and 44.0%, respectively). The main oxygenated monoterpenes were 1, 8-cineole (MEO = 30.0% and REO = 37.0%) and camphor (REO = 12.5%). However, it is noteworthy to note that the main oxygenated derivative in REO was 1,8-cineole (37.0%) (Sharma et al., 2020).

3.2. FT-IR spectral analysis

The FT-IR spectra (4000–400 cm^{-1}) obtained for MEO and REO and the specific band positions and intensities were considered in Fig. 2a and b, respectively. They show some characteristic key bands, which can be used for discrimination between the main volatile substances occurring in MEO and REO such as 1,8- cineole, camphor and α-pinene. Table 2 presents the FT-IR absorption bands for both oils and their vibration assignments compared to literature data (Szymanska-Chargot and Zdunek, 2013). The functional groups identification was based on the FT-IR peaks attributed to stretching and bending vibrations.

The vibrational spectra of MEO in Fig. 2a were dominated by bands of its main components: α-pinene (at 843.48 and 787.29 cm^{-1}) and 1,8-cineole (at 1375.47; 1234.10; 1080.01; 995.84 and 843.48 cm^{-1}). These bands showed characteristic signals in the FT-IR spectrum due to wagging vibrations of CH and CH_2 groups (995.84 cm^{-1} for 1,8-cineole and 843.48 cm^{-1} for α-pinene). Therefore, characteristic but less intensive bands of 1,8-cineole occurring in the FT-IR spectrum were assigned to C-O-C symmetrical (1080.01 cm^{-1}) and asymmetrical (1234.10 cm^{-1}) stretching vibrations. An additional band was observed at 3383.67 cm^{-1}, which could be assigned to a stretching vibration of hydroxyl group. These characteristic key absorption bands mentioned above are in agreement with those reported in previous publications interpreting vibrational spectra of essential oils isolated from Myrtaceae species (Baranska et al., 2006, 2005; Wang and Sung, 2011). In Fig. 2b, the FT-IR spectrum of REO exhibits various characteristic peaks. All the above-mentioned components contribute

Table 1 Volatils compounds composition of MEO and REO.

Compounds	LRI	RT (min)	MEO	REO
propyl butyrate	898	4.24	0.7	–
Tricyclene	928	4.46	–	0.2
α-thujene	933	4.55	0.4	–
α-pinene	941	4.72	40.4	11.6
Camphene	955	5.07	0.2	4.5
β-pinene	982	5.77	0.6	3.1
Myrcene	993	6.14	0.2	1.5
isobutyl 2-methylbutyrate	1002	6.46	0.9	–
α-phellandrene	1006	6.54	–	0.2
δ-3-carene	1013	6.71	0.7	0.5
2-methylbutyl isobutyrate	1015	6.87	0.3	–
α-terpinene	1019	6.92	–	0.4
p-cymene	1028	7.18	2.0	2.1
Limonene	1032	7.31	4.3	2.1
1,8-cineole	1034	7.40	30.0	37.0
γ-terpinene	1062	8.30	0.3	0.3
Terpinolene	1090	9.36	0.4	0.4
Linalool	1101	9.83	2.0	0.7
2-methylbutyl 2-methylbutyrate	1103	9.93	1.9	–
endo-fenchol	1112	10.35	–	0.1
trans-pinocarveol	1141	11.31	0.4	–
Camphor	1145	11.50	0.4	12.5
Borneol	1168	12.43	–	4.9
4-terpineol	1179	12.90	0.6	1.1
α-terpineol	1191	13.51	3.5	2.9
linalyl acetate	1259	16.24	1.0	–
bornyl acetate	1287	17.49	–	0.3
exo-2-hydroxycineol acetate	1345	19.95	0.2	–
α-terpinyl acetate	1352	20.27	1.7	–
α-ylangene	1373	21.15	–	0.2
α-copaene	1377	21.35	–	0.8
geranyl acetate	1383	21.85	4.2	–
β-caryophyllene	1419	23.18	1.2	8.0
Aromadendrene	1441	24.01	–	0.1
α-humulene	1455	24.62	0.2	1.0
γ-muurolene	1477	25.65	–	0.6
β-selinene	1486	26.01	–	0.1
Viridiflorene	1495	26.39	–	0.2
α-muurolene	1499	26.64	–	0.3
trans-γ-cadinene	1513	27.19	–	0.5
δ-cadinene	1524	27.59	–	1.2
germacrene B	1557	28.88	0.1	–
caryophyllene oxide	1582	29.95	0.3	0.4
Monoterpene hydrocarbons	–	–	49.5	26.9
Oxygenated monoterpenes	–	–	44.0	59.5
Sesquiterpene hydrocarbons	–	–	1.5	13.0
Oxygenated sesquiterpene	–	–	0.3	0.4
Non-terpene derivatives	–	–	3.8	0.0
Total identified	–	–	99.1	99.8

Linear retention index (LRI); Retention time (RT).

to C–H stretching bands from 2966.84 to 2881.16 cm^{-1} (in the functional group region), as well as at 1446.82 and 1375.22 cm^{-1}. The peak observed at 1740.63 cm^{-1} is mainly attributed to the keto group of camphor, while peaks at 1214.95 and 991.97 cm^{-1} are because of ether function from the epoxy ring of 1,8-cineole. Finally, the peaks at 1079.65 and 1053.48 cm^{-1} are associated with C–O bond asymmetric stretching. The peak at 3472.13 cm^{-1} is associated with the main IR band, and specifically the O–H stretch, of ethanol group of α-terpineol, 4-terpineol, borneol, linalool and trans pinocarveol. These results are in agreement with a previously published study (Stramarkou et al., 2020).

3.3. Electrochemical studies

3.3.1. Potentiodynamic polarization between −0.4 and + 0.4 V/ SCE

The open circuit potential (OCP) and polarization curves obtained on a large potential range in the diverse MEO and

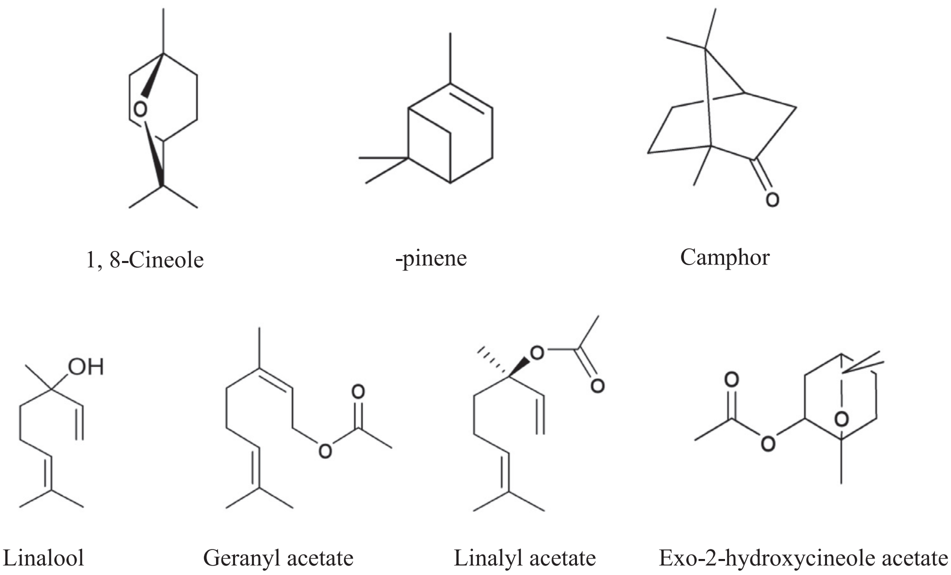

Fig. 1 Chemical structure of the major constituents of EOs.

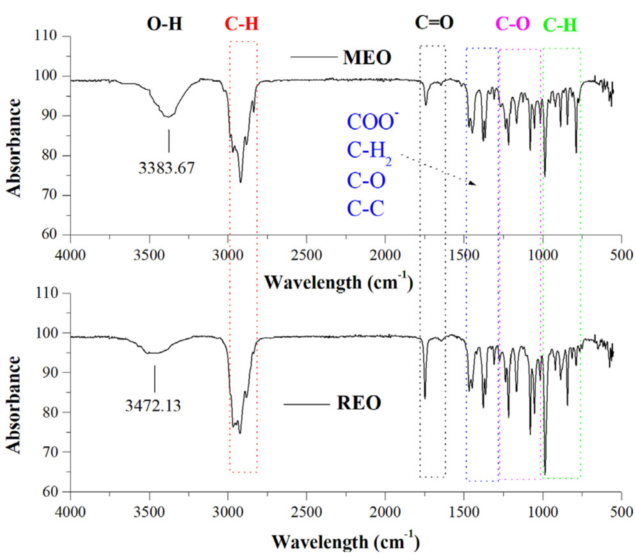

Fig. 2 FT-IR spectra (4000–400 cm^{-1}) obtained for MEO (a) and REO (b).

Table 2 The FT-IR vibration band positions and their assignments for MEO and REO.

Band position (cm^{-1}) MEO	REO	Assignments
3383.67	3472.13	O–H stretching bands
2968.25	2966.84	C–H stretching bands specific to CH_3 and CH_2
2918.54	2923.37	
2880.90	2881.16	
2835.04		
1740.62	1740.63	C=O stretching bands, COO^- antisymmetric stretching
1634.76	1643.46	
1466.16	1465.81	C–O stretching bands and C–C stretching from phenyl groups, COO^- symmetric stretching, CH_2 bending
1446.27	1446.82	
1375.47	1375.22	
1363.96	1361.57	
1306.49	1306.49	
1234.10	1272.92	C–O symmetric stretching bands
	1234.30	
	1214.95	
1125.63	1167.52	C–O asymmetric stretching bands
1080.01	1079.65	
1053.71	1053.48	
1015.50	1016.33	
995.84	991.97	C–H out-of-plane blending bands from isoprenoids
953.08	920.56	
920.54	886.79	
843.48	843.22	
787.29	787.62	
771.82		

REO concentrations (1.25 g/L, 2.5 g/L, 5 g/L, and 10 g/L) are shown in Figs. 3 and 4. They are compared to the curve obtained in similar conditions in a 3 wt% NaCl solution without essential oils, which is referred to as "blank". It can be clearly seen from Figs. 3a and 4a that in any case, the OCP is stable after less than 15 min. So even after 30 min it seems that the system has reached stationary conditions. Besides, the OCP values of the copper substrate move in the negative direction after the addition of the EOs. This indicates that the MEO and REO molecules are likely to have a greater inhibitory effect on the cathodic reaction than the anodic reaction. Figs. 3b and 4b depict that the cathodic branch of the copper in the blank NaCl solution can be divided into three regions : Region I corresponds to the weak polarization region near OCP; Region II is associated with the reduction of dissolved oxygen (Eq. (1)); and Region III (below − 380 mV) is attributed to the hydrogen evolution rection given in Eq. (2) (Huang et al., 2020; Liao et al., 2011).

$$O_2 + 2H_2O + 4e^- \rightarrow 4OH^- \quad (1)$$

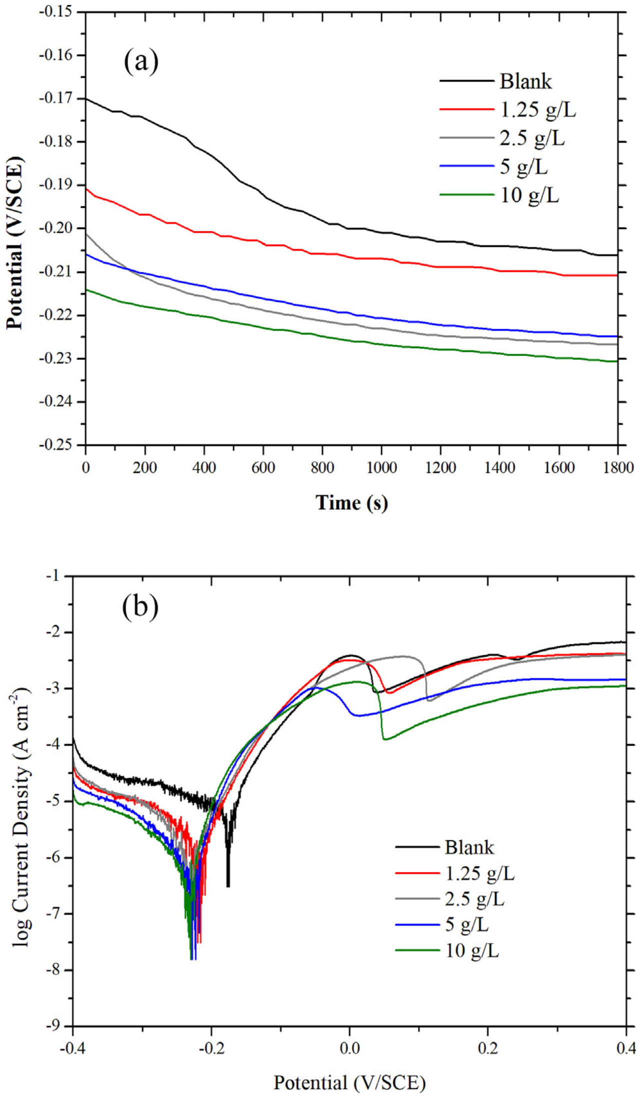

Fig. 3 Open circuit potential plots (a) and potentiodynamic polarization curves (b) for copper electrode in NaCl 3 wt% solution without (blank) and with various concentrations of MEO.

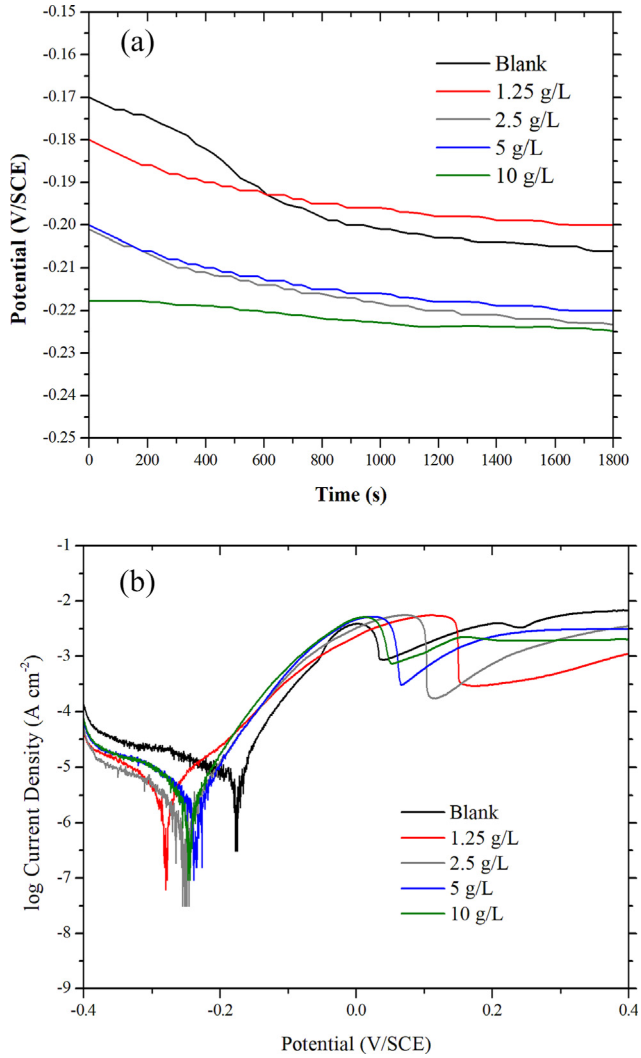

Fig. 4 Open circuit potential plots (a) and potentiodynamic polarization curves (b) for copper electrode in NaCl 3 wt% solution without (blank) and with various concentrations of REO.

$$2H_2O + 2e^- \rightarrow H_2 + 2OH^- \tag{2}$$

The anodic reaction was controlled by both metal electro-dissolutions and metal soluble diffusion in the bulk solution (Khaled, 2010). As can be more described in our previous research work, the dissolution mechanism can be represented by the following reactions (Masmoudi et al., 2014):

$$Cu \rightarrow Cu^+ + e^- \tag{3}$$

$$Cu + Cl^- \rightarrow CuCl + e^- \tag{4}$$

$$CuCl + Cl^- \rightarrow CuCl^-_{2(surface)} \tag{5}$$

In the presence of EOs, the oxygen diffusion-limited current density (region II) decreases, emanating from the reduction of oxygen dissolution rate and indicating a decrease in the corrosion rate. However, the cathodic branches' shape is not changed, confirming the fact that a simple corrosion mechanism happened in NaCl corrosion solution. The parallel cathodic branches depicted the unchanged hydrogen evolution mechanism even at high OEs concentration. For the anodic branch, the current density is practically not changed. As a result, polarization curves are almost parallel region, indicating that modifying copper surface does not change cathodic and anodic reactions. Moreover, the corrosion potentials (E_{corr}) shifted to more negative values in the presence of REO and MEO, thus confirming that these oils have a stronger influence on oxygen cathodic reduction than on copper oxidation reaction. The E_{corr} values measured for the blank, 1.25 g/L, 2.5 g/L, 5 g/L and 10 g/L MEO solutions are equal to −175, −220, −230, −225 and −237 mV/SCE respectively. Besides, these values measured for 1.25 g/L, 2.5 g/L, 5 g/L and 10 g/L REO solutions are respectively equal to −225, −242, −280 and −255 mV/SCE. Hence, the E_{corr} shift reaches 62 mV for the highest concentration (10 g/L) of MEO and 105 mV for 5 g/L concentration of REO, which is a sufficiently high value to classify the EOs as a cathodic inhibitor rather than a mixed inhibitor (Sherif, 2012).

Finally, the minimum current density is lesser than that obtained in the blank solution. This indicates that the adsorption of the inhibitor is more likely to hinder the formation of the adsorbed species (reaction (5)), preventing the dissolution of the CuCl film and/or favoring its formation.

3.3.2. Voltammetry around OCP ($\Delta E = \pm 50$ mV)

To further determine the REO and MEO corrosion resistance performance in various concentrations, potentiodynamic polarization tests were realized after 20 min of immersion in 3 wt% NaCl on a limited potential range ($\Delta E = \pm 50$ mV). Fig. 5a and b show examples of the experimental polarization curves of MEO (1.25 g/L) and REO (1.25 g/L), respectively, and Tafel curves simulated with EC-Lab software (Bio-Logic). This latter is useful for calculating various corrosion parameters, such as corrosion current densities (J_{corr}), Tafel slope constants (β_a and β_c), polarization resistance (R_p) and corrosion rate (CR).

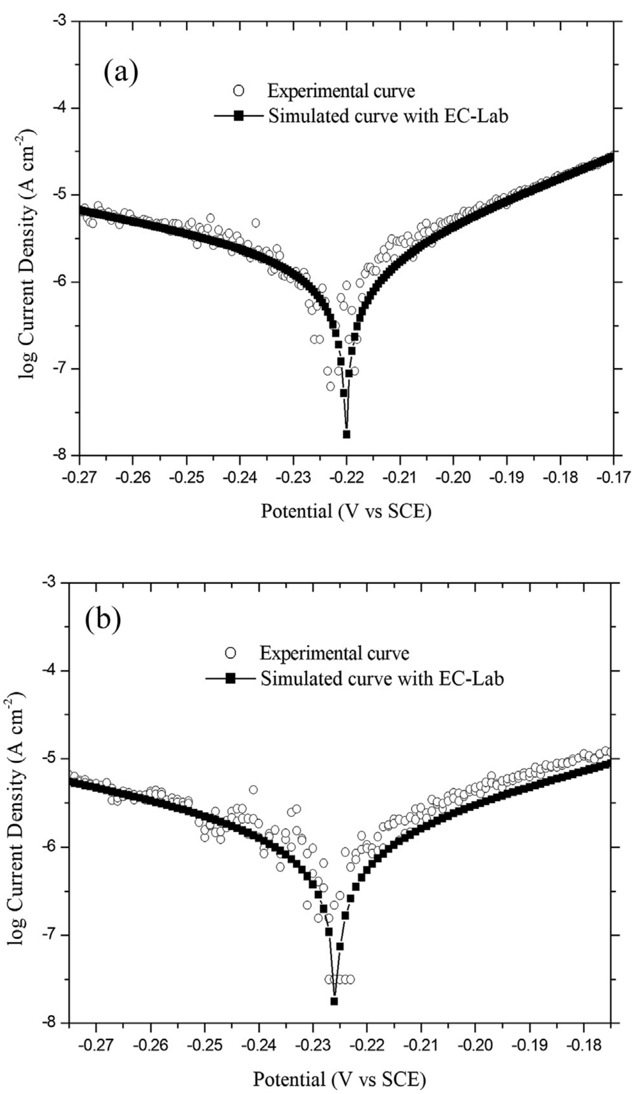

Fig. 5 Experimental polarization curve around OCP of MEO (a) and REO (b) for 1.25 g/L in 3 wt% NaCl solution and computed curve.

The efficiency of the inhibition (η %) is then calculated by the next formula:

$$\eta\% = \frac{J^0{}_{corr} - J_{corr}}{J^0{}_{corr}} \times 100$$

where $J^0{}_{corr}$ and J_{corr} represent the corrosion current densities without and with inhibitor addition, respectively.

All the electrochemical parameters (fitting by EC-Lab software) are listed in Table 3.

In the used experimental conditions, the cathodic branch represents the reactions of oxygen reduction and the anodic branch corresponds to the copper dissolution (Elmorsi and Hassanein, 1999). It can be noted that in the presence of the MEO and REO, the anodic Tafel slopes (β_a) have approximately constant around an average value of 35 and 44 mV decade^{-1}, respectively. These values accord well with those found for copper static electrodes in aerated neutral 3.0–3.5% g/L NaCl solutions ranging between 45 and 60 mV decade^{-1} (Rahal et al., 2016). This result indicates that the presence of EOs has no significant impact on the copper dissolution. Nevertheless, the cathodic Tafel slopes (β_c), decreases sharply with the REO and MEO addition, which may be explained by the presence of the inhibitors involving delay in the oxygen reduction.

As can be seen from Table 3, the values of J_{corr} decrease gradually with the increase of MEO and REO concentrations. The decrease in J_{corr} value emanates essentially from the decrease of the cathodic reaction rate. In particular, J_{corr} of REO at 10 g/L is 13-fold lower (0.509 μA.cm^{-2}) than 6.83 μA.cm^{-2} obtained in the blank solution. Besides, REO can be said to have relatively less corrosion current densities (J_{corr}) than obtained with MEO. As a result, the corrosion rate decreases strongly with the increase in the EOs concentrations, reaching a minimum value of 6.42 10^{-3} mm/year and 5.9 10^{-3} mm/year at 10 g/L for MEO and REO, respectively. Furthermore, the inhibition efficiency, η, reached 91.88% and 92.54% at 10 g/L concentrations for MEO and REO, respectively. This confirms that EOs show a good inhibition effect on copper in 3 wt% NaCl and the high EOs' concentration could enhance protection ability against copper corrosion.

3.3.3. Electrochemical impedance spectroscopy (EIS)

Fig. 6a and b display the Nyquist diagrams of copper in 3 wt% NaCl solution, in the absence (blank) and the presence of various concentrations of MEO and REO, respectively, at 25 °C.

The Nyquist plot of the copper in the blank solution presents a depressed capacitive semicircle in the high-frequency region and a straight line (Warburg impedance) in the low-frequency region. The semicircle in the high-frequency region represents the combination of charge-transfer resistance (R_{ct}) and the double-layer capacitance (Q_{dl}). The low-frequency straight line portion is the indication of a diffusion-controlled corrosion process occurring on the copper surface (Sherif, 2012). This diffusion process can be accredited to the anodic diffusion process of soluble copper species ($CuCl_2^-$) from the electrode surface to the bulk solution, and the cathodic diffusion process of dissolved oxygen from the bulk solution to the surface of the electrode (Hassairi et al., 2013; Hong et al., 2013; Khaled, 2009; Liao et al., 2011).

The Nyquist plots of MEO and ROE (Fig. 6a and b) show two depressed capacitive loops which are not always clearly

Table 3 Electrochemical kinetic parameters and inhibition efficiency obtained from potentiodynamic polarization curves ($\Delta E = \pm 50$ mV) of copper electrode immersing in 3 wt% NaCl solutions without (blank) and with various concentrations of MEO and REO at RT (~25 °C).

	Cc (g/L)	J_{corr} ($\mu A.cm^{-2}$)	$-\beta_c$ (mV/dec)	β_a (mV/dec)	R_p ($k\Omega\ cm^2$)	CR (mm/year)	η(%)
Blank		6.83	199	43	2.247	0.079	–
MEO	1.25	1.665	82.3	40.8	7.11	0,019	75.62
	2.5	1.294	40	34.9	6.25	0.015	81.05
	5	0.677	38.7	32.2	11.27	$7.88\ 10^{-3}$	90.08
	10	0.554	41.8	32.6	14.35	$6.42\ 10^{-3}$	91.88
	1.25	1.389	80.3	62.2	10.97	0.016	79.66
REO	2.5	0.901	50	37.2	10.29	0.010	86.80
	5	0.656	59.8	45.5	17.12	$7.6\ 10^{-3}$	90.39
	10	0.509	39.5	33.8	15.55	$5.9\ 10^{-3}$	92.54

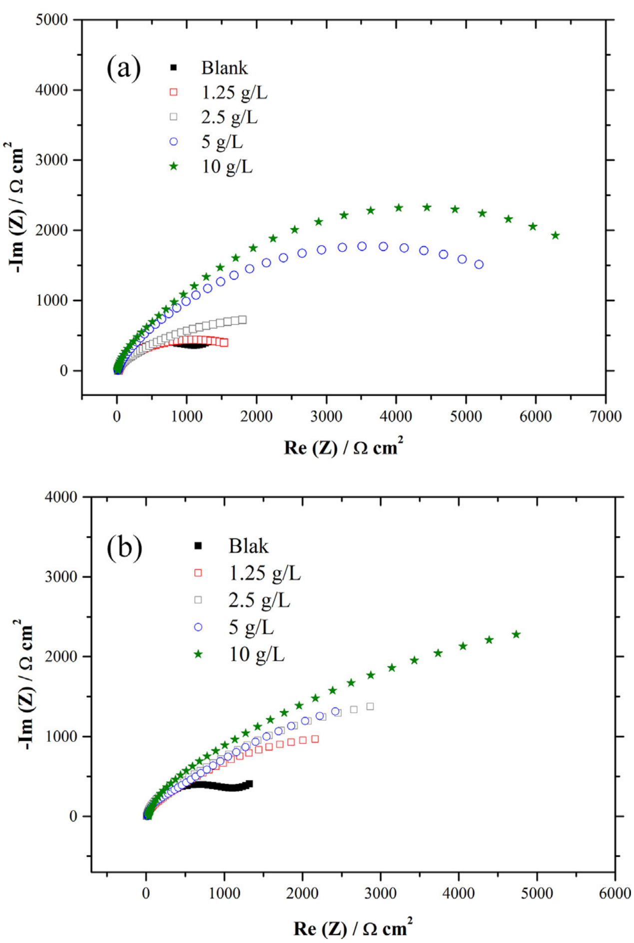

Fig. 6 Nyquist plots for copper electrode immersion in NaCl 3 wt% solution without (blank) and with various concentrations of MEO (a) and REO (b).

separated (i.e., they appear to be a single capacitive loop). The diameter of these capacitive loops increases with the increase of the EOs concentration, indicating an improvement of a more capacitive surface film, promoting the formation of the protective layer. The observed depressed semicircle with the center under the real axis, is due to non-homogeneities and other roughness on the metal surface at the interface (Karthik et al., 2017). The capacitive loop at the high-frequency region is ascribed to the contribution of the film formed on the surface, and the capacitive loop at the medium frequency region is ascribed to the charge transfer reaction at electrode/solution interface (Boudellioua et al., 2019). When the EOs concentrations are 1.25 and 2.5 g/L, the Warburg impedance was also observed in the low-frequency region related to mass transport, i.e. more likely O_2 diffusion. In contrast, for the EOs concentrations 5 and 10 g/L, the time constant disappeared in the low-frequency region, suggesting that the formed film was densely packed to impede the diffusion process involved in the corrosion reaction (Karthik et al., 2017).

Fig. 7a and b correspond to bode plots (log |Z| as function of the log f) of copper in 3 wt% NaCl solution without and with MEO and REO, respectively. They basically show three well-distinguished regions: (i) the high-frequency zone, where the log |Z| values are lowest and present an almost horizontal straight line. This is a typical response for resistive behavior and represents the solution resistance; (ii) a linearity between the log |Z| and the log f values is observed in the medium frequencies (iii) afterward, a low-frequency region, where the log |Z| formed an inclined straight line with a negative slope. The |Z| value of the copper in the blank solution at 0.1 Hz is 1258 $\Omega.cm^2$, suggesting that the substrate easily corrodes (small polarization resistance). However, in the same frequency, this value became 6309 $\Omega.cm^2$ for the higher inhibitor concentration (10 g/L) of MEO and REO. This confirmed that a considerable boost of corrosion protection was achieved by the addition of EOs in the electrolyte.

The phase angle plots (Fig. 7c and d) for copper in blank NaCl solution shows two relaxation time constants: the first one at the high-frequency region, is related to the relaxation process of electrical double layer capacitor and charge-transfer, and the second at low-frequency region corresponding to Warburg diffusion (corrosion process). Besides, it is evident that the phase angles were close to −57 for the blank, to −70 for MEO and to −68 for REO at a concentration of 10 g/L in a wide frequency region, which indicates retardation of corrosion process (Pareek et al., 2019). In addition, the low frequencies diffusive impedance is related to the diffusion of corrosive species, such as dissolved oxygen. Particularly, Warburg

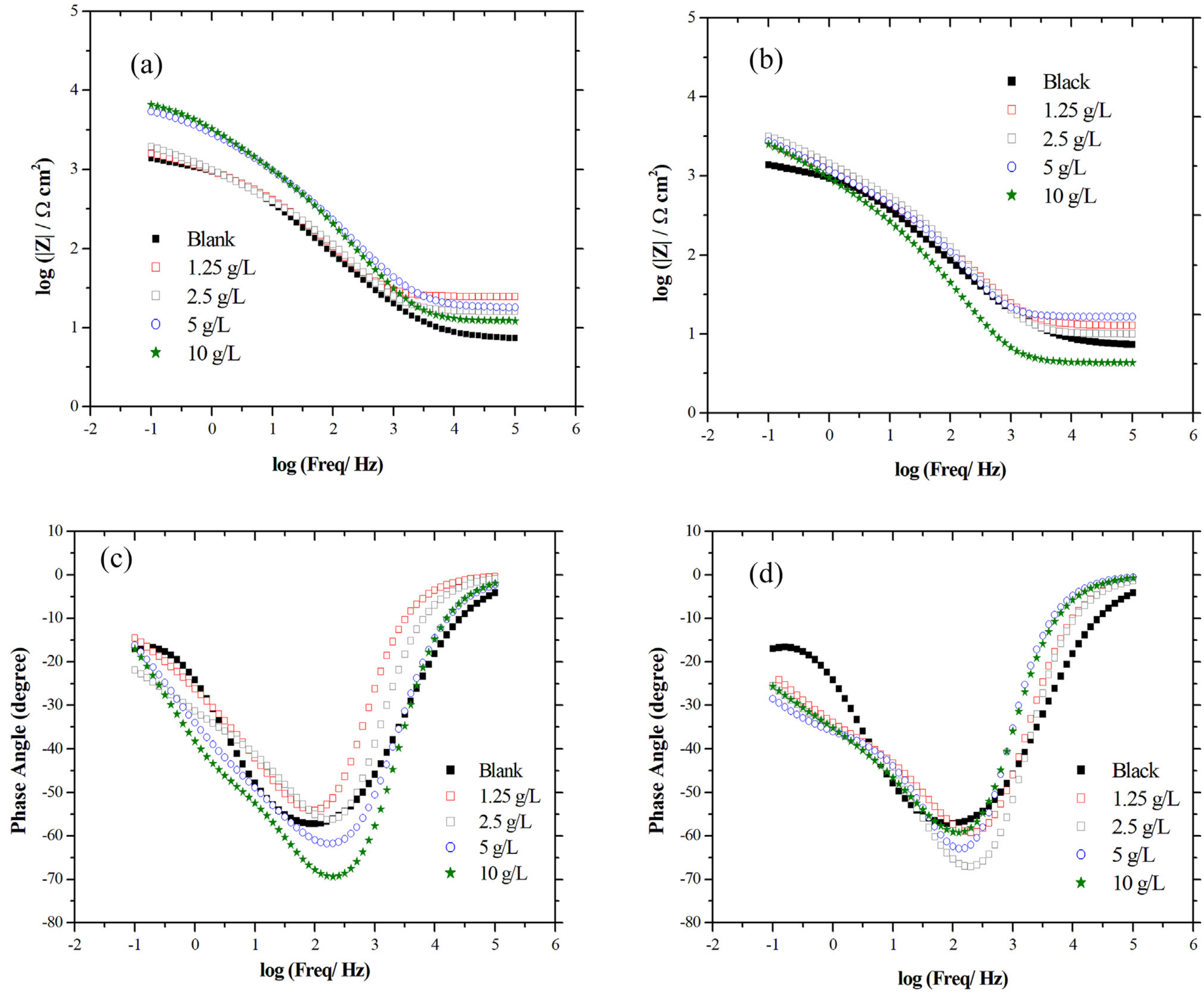

Fig. 7 Bode plots impedance modulus versus frequency for MEO (a), REO (b) in 3 wt% NaCl medium, phase angle versus frequency plots for MEO (c) and REO (d) in 3 wt% NaCl medium.

impedance disappears in the high concentrations of MEO and REO as demonstrated in Fig. 7c and d, respectively. Consequently, EOs with higher concentrations (5 g/L and 10 g/L), was proven to form a stable layer over the copper surface that acted as an effective barrier to provide corrosion protection.

Fig. 8 exhibits the electrochemical equivalent circuit models used to fit the experimental results is to obtain the quantitative assessment of the EIS data. Three electric equivalent circuits (EEC) was considered and these models have been used in various studies to describe the behavior of copper in chloride-containing solutions, without or with inhibitors (Hassairi et al., 2013; Hong et al., 2013; Khaled, 2009). Among all the elements involved in the equivalent circuits, R_s is the resistance of the solution between the reference electrode and the working electrode; R_f is the resistance of the protective inhibitor film formed on copper surface; R_{ct} is the charge transfer resistance between the solution and the metal surface interface; Q_{dl} corresponds to the double layer capacitance (Q_{dl}); Q_f is composed to the film capacitance, and W is Warburg resistance (Refait et al., 2020). In impedance spectroscopy practice, several experimental results show a frequency distribution of the parameters. The latter determined the necessity of a modeling element with frequency dispersion behavior. The impedance of constant phase element (CPE) is described by this relationship: (Annibaldi et al., 2012; Refait et al., 2020)

$$Z_{CPE} = 1/Q_0(j\omega)^n$$

where Q_0 is the magnitude of CPE, j is the imaginary root, ω is the angular frequency, and n value is attributed to the inhomogeneous nature of the electrode due to surface roughness, porous layer formation, inhibitor adsorption, etc.

Fig. 8a proves suitable for the experimental impedance data of copper in the blank solution. In this model, the electric equivalent circuit contains R_s, R_{ct}, Q_{dl} and W. This shows that the contribution of the film of corrosion products formed on the metal surface is negligible. In contrast, the equivalent circuits used for copper in solutions containing REO and MEO (Fig. 8b and c) include a contribution of the film of corrosion products via the resistance R_f and the element Q_f.

The equivalent circuit in Fig. 8b which includes Warburg impedance is used for less concentrations 1.25 and 2.5 g/L of MEO and REO. The equivalent circuit of Fig. 8c which does not include Warburg impedance is used for high concentrations of EOs (5 and 10 g/L).

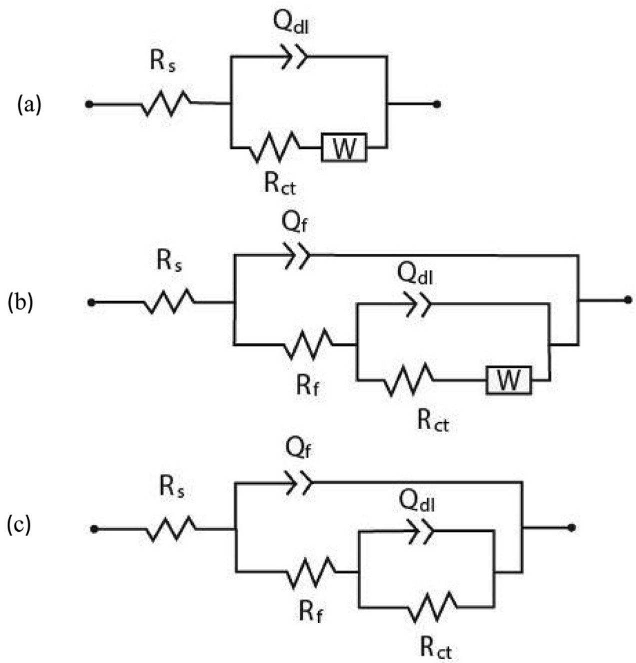

Fig. 8 Equivalent circuits used to fit the EIS experimental data.

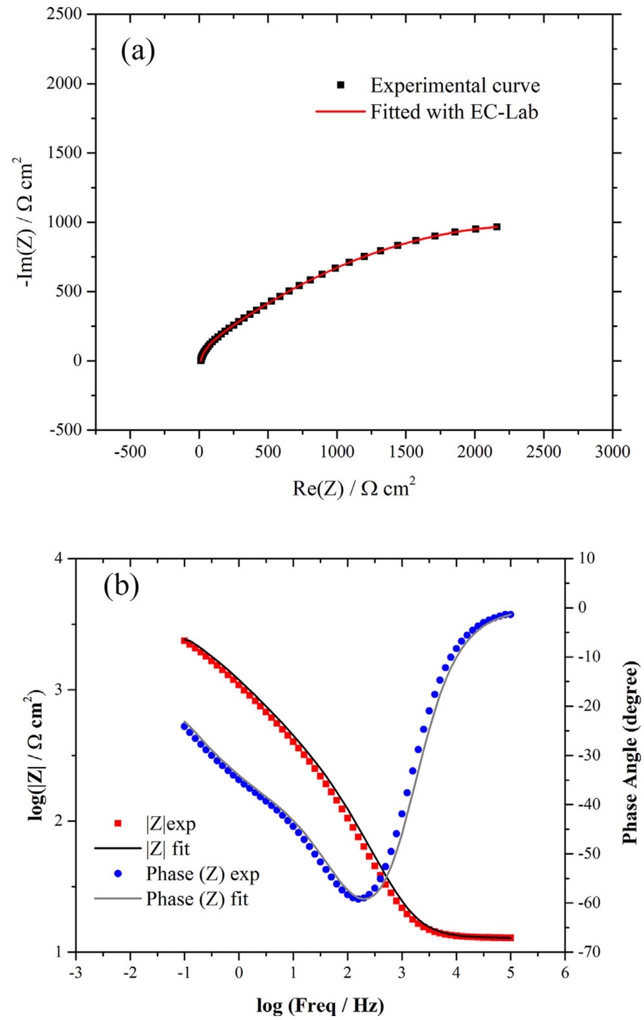

Fig. 9 Experimental Nyquist (a) and Bode (b) plots and their mathematical fitting: Example of copper in 3 wt% NaCl solution with REO concentration of 1.25 g/L. Circles and squares (phase): experimental curves, lines: computed curves.

An excellent agreement was obtained between experimental and fitted results (χ^2 values nearly equal to 1×10^{-3}, χ^2 values is the sum of the square of the difference between experimental and theoretical values). A typical example of the results given by experimental measurements and the computer fittings is presented in Fig. 9. The model shows a good agreement with the experimental results for both Nyquist and Bode plots, shown in Fig. 9a and b, respectively. The results obtained after the computer fitting of the experimental impedance data are listed in Table 4.

Apparently, the values of Q_f and Q_{dl} of the two EOs at 10 g/L are the lowest, which indicate that fewer corrosion products were formed due to the lack of active sites (López et al., 2008). The values of n_f and n_{dl} are usually related to the roughness of the electrode surface; the smaller the n value, the higher the surface roughness (Amin et al., 2010; Barsoukov and Macdonald, 2005). The constant n_f values, which are close to 1, show an important density of the film formed on the surface of copper. For 1.25 and 2.5 g/L concentrations, the values of Warburg (W) confirm the mass transport of oxygen, which is in accordance with the derived values of the capacitance and protection efficiency. Moreover, the appearance of the Warburg impedance of these concentrations could be ascribed to the NaCl solution penetration in the film defects.

The inhibition efficiency η was computed according to (Rahal et al., 2016; Refait et al., 2020):

$$\eta\ (\%) = \frac{R_p - R_p^0}{R_p} \times 100$$

where R_p^0 and R_p are total polarization resistance of copper in the solution without and with inhibitors, respectively, and R_p is the sum of R_f and R_{ct}.

The R_{ct} value increased from 2.380 kΩ.cm² to 7.763 kΩ.cm² in the MEO solution and from 4.667 kΩ cm² to 13.449 kΩ cm² in the REO solution at concentrations from 1.25 g/L to 10 g/L. R_f was found to increase along with the EOs concentration, revealing that the increase of corrosion inhibition effect is closely related to the important protectiveness of surface film when inhibitor concentration is higher than1.25 g/L.

The polarization resistance R_p for MEO at 10 g/L was found to be 7-fold higher than that of R_p^0, and 12-fold higher than that of R_p^0 for REO at 10 g/L. Consequently, the values of inhibition efficiency augment with the increase in the concentration of the inhibitors, reaching 86.78% for MEO and 91.74% for REO at a concentration of 10 g/L. These results accord well with those obtained from the polarization measurements, which reveal that REO has relatively superior performance in inhibiting the corrosion of copper in saline environment compared to MEO.

3.4. Adsorption isotherms modelling

The major step in the corrosion inhibition process is determined by the adsorption of inhibitors on the substrate surface (Rudresh and Mayanna, 1977). It is widely recognized that organic molecules inhibited corrosion by adsorption at the

Table 4 Electrochemical parameters and inhibition efficiency obtained from EIS study of copper electrode immersing in 3 wt% NaCl solutions without (blank) and with various concentrations of MEO and REO at RT (~25 °C).

		Blank	MEO 1.25 g/L	MEO 2.5 g/L	MEO 5 g/L	MEO 10 g/L
MEO	Rs (Ω cm^2)	7.13 ± 0.3	24.8 ± 2	16.1 ± 0.2	17.9 ± 0.4	12.14 ± 0.02
	R_{ct} (Ω cm^2)	1137 ± 80	2380 ± 700	3230 ± 300	6621 ± 200	7763 ± 800
	$Q_{dl}.10^{-6}$ (F cm$^{-2}s^n_{dl}$)	110 ± 20	312 ± 80	368 ± 100	94 ± 40	77 ± 4
	n_{dl}	0.72 ± 0.4	0.42 ± 0.02	0.46 ± 0.1	0.53 ± 0.05	0.60 ± 0.06
	R_f (Ω cm^2)	–	11.3 ± 2	161.6 ± 30	766.3 ± 75	840.0 ± 70
	$Q_f.10^{-6}$ (F cm$^{-2}s^n_f$)	–	13.35 ± 2	20.45 ± 3.3	17.55 ± 1.8	13.05 ± 0.8
	n_f	–	0.975 ± 0.01	0.914 ± 0.02	0.842 ± 0.001	0.908 ± 0.011
	W (Ω^{-1} cm^{-2} s$^{0.5}$)	244.5 ± 18	3.7 ± 3	150.4 ± 15	–	–
	η (%)	–	52.45	66.47	84.61	86.78
REO	Rs (Ω cm^2)	7.1 ± 0.3	12.8 ± 0.2	10.1 ± 0.8	16.5 ± 1	32.3 ± 2.2
	R_{ct} (Ω cm^2)	1137 ± 80	4667 ± 400	6087 ± 480	7186 ± 600	13449 ± 900
	$Q_{dl}.10^{-6}$ (F cm$^{-2}s^n_{dl}$)	110 ± 20	306 ± 70	267 ± 80	351 ± 40	165 ± 9
	n_{dl}	0.72 ± 0.4	0.48 ± 0.03	0.50 ± 0.02	0.49 ± 0.08	0.43 ± 0.06
	R_f (Ω cm^2)	–	229.1 ± 28	382.1 ± 30	263.0 ± 7	312.6 ± 38
	$Q_f.10^{-6}$ (F cm$^{-2}s^n_f$)	–	22.42 ± 3	19.16 ± 2.2	17.36 ± 1.9	11.10 ± 2.1
	n_f	–	0.889 ± 0.01	0.923 ± 0.01	0.962 ± 0.02	0.922 ± 0.002
	W (Ω^{-1} cm^{-2} s$^{0.5}$)	244.5 ± 18	6.2 ± 4	158.7 ± 12	–	–
	η (%)	–	76.77	82.42	84.73	91.74

metal/solution interface. In the aim of determining inhibitors adsorption characteristics, several attempts on various isotherms were realized namely Langmuir, Frumkin, Temkin, Freundlich, and Flory-Huggins (Daoud et al., 2015; Khaled, 2008).

Surface coverage ($\theta = \eta(\%)/100$) for different concentrations of EOs in 3 wt% NaCl solution was evaluated from the results of voltammetry around OCP. Fitting the θ values as a function of the EOs concentration (g/L) was carried out to propose a suitable adsorption mechanism and the correlation coefficient (R^2) is used to choose the isotherm that best fits the experimental data. As can been seen in the Table 5 and Fig. 10, the R^2 of Langmuir is closer to 1 than other fittings (0.9998 for MEO and 1 for REO). Therefore, Langmuir adsorption isotherm is the most suitable candidate to explain the adsorption relationship between EOs molecules and the copper surface, according to Equation:

$$\frac{C}{\theta} = \frac{1}{K_{ads}} + C$$

where K_{ads} is the equilibrium constant of the adsorption–desorption process (g^{-1}.L).

Based on the theory of Langmuir adsorption isotherm, it can infer that all EOs molecules have equal opportunities to

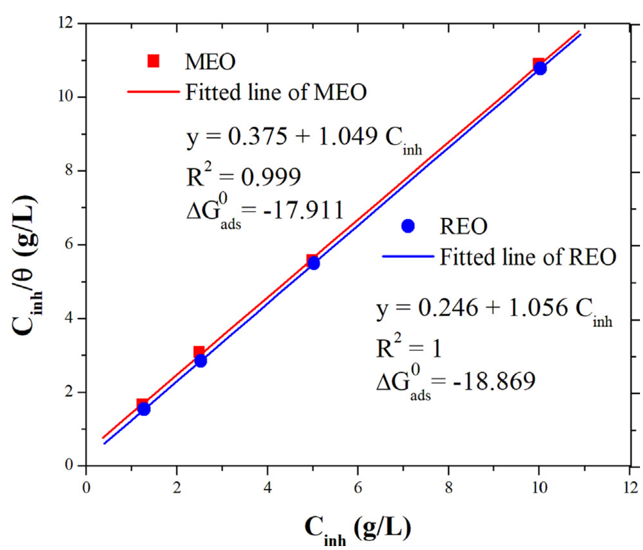

Fig. 10 Langmuir adsorption isotherms for MEO and REO on the copper surface.

Table 5 Adsorption Isotherm modeling of MEO and REO in 3 wt% NaCl solution at 25 °C.

Isotherm	Linear form of Isotherm	Plot	R^2 MEO	R^2 REO
Langmuir	$\frac{C}{\theta} = \frac{1}{K_{ads}} + C$	$\frac{C}{\theta}$ vs. C	0.999	1
Frumkin	$\ln[\frac{\theta}{(1-\theta)C}] = 2a\theta + \ln K_{ads}$	$\ln\left[\frac{\theta}{(1-\theta)C}\right]$ vs. θ	0.811	0.906
Temkin	$\ln C = a\theta - \ln K_{ads}$	$\ln C$ vs. θ	0.973	0.965
Freundlich	$\log\theta = n\log C + \log K_{ads}$	$\log\theta$ vs. logC	0.972	0.960
Flory–Huggins	$\log\frac{\theta}{C} = \log(xK_{ads}) + x\log(1-\theta)$	$\log\frac{\theta}{C}$ vs. $\log(1-\theta)$	0.972	0.974

adsorb on the copper surface, and then form a monolayer organic anti-corrosion film. Meanwhile, the adsorbed molecules occupy only one site and no interactions exist between the adsorbed species. Furthermore, no other reactions occur on the copper surface except for adsorption and desorption (Foo and Hameed, 2010; Masmoudi et al., 2015). The inspection of the chemical structures displayed in Fig. 1 demonstrates that the oxygen atoms almost surround the aromatic rings of the EOs. This arrangement of the oxygen atoms has proven that these compounds are forced to be adsorbed onto the copper surface (Li et al., 2014).

The standard of free energy adsorption (ΔG^0_{ads}) is calculated according to (Honarvar Nazari et al., 2017):

$$\Delta G^0_{ads} = -RT\ln(1000K_{ads})$$

were, R is the molar gas constant (8.314 J $mol^{-1}K^{-1}$), T is the absolute temperature (298.15 K), and 1000 is the water concentration (g/L).

The Gibbs free energy was estimated to be −17.91 $kJmol^{-1}$ for MEO and −18.87 for REO. The negative values of ΔG^0_{ads}suggested the spontaneous occurrence of adsorption process of EOs species onto the copper surface. They also indicate the strong interaction and stability of the adsorption layer with the copper surface (Solmaz, 2014). Three approaches of adsorption may happen through the inhibition of the EOs molecules at the copper/solution interface (Shalabi et al., 2020): (a) Electrostatic interaction between the inhibitor molecules and the metallic surface (i.e., physisorption), (b) Coordination between the lone pair of O atoms or π-electrons cloud and the metallic surface (i.e., chemisorption), (c) Happening both above explanations. The absolute values of ΔG^0_{ads} were smaller than 20 $kJmol^{-1}$, which suggested that the adsorption mechanism of the EOs on copper surface in 3 wt% NaCl solution is a typical physisorption: approach a (vs. chemical adsorption). The number of chemical components in this extract (Table 1) leads to the difficulty in understanding the inhibiting effect and its attribution to a particular constituent or group of constituents (Bozorg et al., 2014). Nonetheless, the oxygen atoms in the EOs molecules have high electron density. These sites are nominated to be the active sites to proper electrophiles and can be attached within the metal surface. The inhibitor molecules adsorbed on the substrate by blocking the cathodic active sites on the metal surface, hindering the corrosion reaction (Abbas et al., 2019).

4. Conclusion

By analyzing the obtained OCP and potentiodynamic polarization results, it can be deduced that the EOs act as cathodic type corrosion inhibitors and the corrosion resistance of copper increased with the increase of the concentration of these oils. The inhibition efficiency reached 91.88% and 92.54% at 10 g/L for MEO and REO, respectively. These results are in good agreement with those obtained from EIS, which reveals that REO has moderately stronger adsorption affinity on the copper surface and exhibits relatively better inhibitive performance compared to MEO: η equal 86.78% for MEO and 91.74% for REO at a 10 g/L. The adsorption of EOs molecules follows the Langmuir isotherm through the physical adsorption in which electrostatic interaction occurs between inhibitor molecules and metal surface.

Declaration of Competing Interest

The authors declare that they have no known competing financial interests or personal relationships that could have appeared to influence the work reported in this paper.

Acknowledgements

The authors thank Professor Flamini, for his precious help with GC-MC analysis.

References

Abbas, M.A., Zakaria, K., El-Shamy, A.M., El Abedin, S.Z., 2019. Utilization of 1-butylpyrrolidinium Chloride Ionic Liquid as an Eco-friendly Corrosion Inhibitor and Biocide for Oilfield Equipment: Combined Weight Loss, Electrochemical and SEM Studies. Z. Phys. Chem. 1.

Ahmed, R.K., Zhang, S., 2019. Alchemilla Vulgaris Extract as Green Inhibitor of Copper Corrosion in Hydrochloric Acid. Int. J. Electrochem. Sci 14, 10657–10669.

Aleksic, V., Knezevic, P., 2014. Antimicrobial and antioxidative activity of extracts and essential oils of Myrtus communis L. Microbiol. Res. 169, 240–254.

Amin, M.A., Khaled, K.F., Mohsen, Q., Arida, H.A., 2010. A study of the inhibition of iron corrosion in HCl solutions by some amino acids. Corros. Sci. 52, 1684–1695.

Ammouchi, N., Allal, H., Zouaoui, E., Dob, K., Zouied, D., Bououdina, M., 2019. Extracts of Ruta Chalepensis as Green Corrosion Inhibitor 8 for Copper CDA 110 in 3% NaCl Medium: Experimental 9 and Theoretical Studies 10.

Annibaldi, V., Rooney, A.D., Breslin, C.B., 2012. Corrosion protection of copper using polypyrrole electrosynthesised from a salicylate solution. Corros. Sci. 59, 179–185.

Asllani, U., 2000. Chemical composition of Albanian myrtle oil (Myrtus communis L.). J. Essent. Oil Res. 12, 140–142.

Baranska, M., Schulz, H., Reitzenstein, S., Uhlemann, U., Strehle, M. A., Krüger, H., Quilitzsch, R., Foley, W., Popp, J., 2005. Vibrational spectroscopic studies to acquire a quality control method of Eucalyptus essential oils. Biopolym.: Original Res. Biomol. 78, 237–248.

Baranska, M., Schulz, H., Walter, A., Rösch, P., Quilitzsch, R., Lösing, G., Popp, J., 2006. Investigation of eucalyptus essential oil by using vibrational spectroscopy methods. Vib. Spectrosc. 42, 341–345.

Barsoukov, E., Macdonald, J.R., 2005. Impedance Spectroscopy Theory, Experiment, and. Applications, 2nd ed. (Hoboken, NJ: John Wiley & Sons, Inc., 2005).

Beikmohammadi, M., Fotouhi, L., Ehsani, A., Naseri, M., 2018. Potentiodynamic and electrochemical impedance spectroscopy study of anticorrosive properties of p-type conductive polymer/ TiO2 nanoparticles. Solid State Ionics 324, 138–143.

Bekkara, F.A., Bousmaha, L., Bendiab, S.A.T., Boti, J.B., Casanova, J., 2007. Chemical composition of essential oil cultivated and wild growing Rosmarinus officinalis L. from Tlemcen (Algeria). Biol. Health 7, 6–11.

Benarioua, M., Mihi, A., Bouzeghaia, N., Naoun, M., 2019. Mild steel corrosion inhibition by Parsley (Petroselium Sativum) extract in acidic media. Egypt. J. Pet. 28, 155–159.

Bouaziz, M., Yangui, T., Sayadi, S., Dhouib, A., 2009. Disinfectant properties of essential oils from Salvia officinalis L. cultivated in Tunisia. Food Chem. Toxicol. 47, 2755–2760.

Boudellioua, H., Hamlaoui, Y., Tifouti, L., Pedraza, F., 2019. Effects of polyethylene glycol (PEG) on the corrosion inhibition of mild steel by cerium nitrate in chloride solution. Appl. Surf. Sci. 473, 449–460.

Bouzabata, A., Cabral, C., Gonçalves, M.J., Cruz, M.T., Bighelli, A., Cavaleiro, C., Casanova, J., Tomi, F., Salgueiro, L., 2015. Myrtus communis L. as source of a bioactive and safe essential oil. Food Chem. Toxicol. 75, 166–172.

Bozorg, M., Shahrabi Farahani, T., Neshati, J., Chaghazardi, Z., Mohammadi Ziarani, G., 2014. Myrtus Communis as Green Inhibitor of Copper Corrosion in Sulfuric Acid. Ind. Eng. Chem. Res. 53, 4295–4303. https://doi.org/10.1021/ie404056w.

Chaudhari, S., Patil, P.P., 2011. Inhibition of nickel coated mild steel corrosion by electrosynthesized polyaniline coatings. Electrochim. Acta 56, 3049–3059.

Cheraif, K., Bakchiche, B., Gherib, A., Bardaweel, S.K., Çol Ayvaz, M., Flamini, G., Ascrizzi, R., Ghareeb, M.A., 2020. Chemical Composition, Antioxidant, Anti-Tyrosinase, Anti-Cholinesterase and Cytotoxic Activities of Essential Oils of Six Algerian Plants. Molecules 25, 1710.

Chraka, A., Raissouni, I., Benseddik, N., Khayar, S., Mansour, A.I., Belcadi, H., Chaouket, F., Bouchta, D., 2020. Aging time effect of Ammi visnaga (L.) lam essential oil on the chemical composition and corrosion inhibition of brass in 3% NaCl medium. Experimental and theoretical studies. Mater. Today: Proc. 22, 83–88.

Cristofari, G., Znini, M., Majidi, L., Bouyanzer, A., Al-Deyab, S.S., Paolini, J., Hammouti, B., Costa, J., 2011. Chemical composition and anti-corrosive activity of Pulicaria mauritanica essential oil against the corrosion of mild steel in 0.5 M H2SO4. Int. J. Electrochem. Sci 6, 6699–6717.

Daoud, D., Douadi, T., Hamani, H., Chafaa, S., Al-Noaimi, M., 2015. Corrosion inhibition of mild steel by two new S-heterocyclic compounds in 1 M HCl: experimental and computational study. Corros. Sci. 94, 21–37.

Elamrani, A., Zrira, S., Benjilali, B., Berrada, M., 2000. A study of Moroccan rosemary oils. J. Essent. Oil Res. 12, 487–495.

Elmorsi, M.A., Hassanein, A.M., 1999. Corrosion inhibition of copper by heterocyclic compounds. Corros. Sci. 41, 2337–2352.

Emembolu, L.N., Onukwuli, O.D., 2019. Corrosion inhibitive efficacy of natural plant extracts on zinc in 0.5 M HCl solution. Pharmaceut. Chem. J. 6, 62–70.

Fang, Y., Suganthan, B., Ramasamy, R.P., 2019. Electrochemical characterization of aromatic corrosion inhibitors from plant extracts. J. Electroanal. Chem. 840, 74–83.

Foo, K.Y., Hameed, B.H., 2010. Insights into the modeling of adsorption isotherm systems. Chem. Eng. J. 156, 2–10.

González-Minero, F.J., Bravo-Díaz, L., Ayala-Gómez, A., 2020. Rosmarinus officinalis L. (Rosemary): An Ancient Plant with Uses in Personal Healthcare and Cosmetics. Cosmetics 7, 77.

Hassairi, H., Bousselmi, L., Khosrof, S., Triki, E., 2013. Evaluation of the inhibitive effect of benzotriazole on archeological bronze in acidic medium. Appl. Phys. A 113, 923–931.

Hcini, K., Sotomayor, J.A., Jordan, M.J., Bouzid, S., 2013. Chemical composition of the essential oil of Rosemary (Rosmarinus officinalis L.) of Tunisian origin. Asian J. Chem. 25, 2601–2603.

Hedayati, S., Niakousari, M., Mohsenpour, Z., 2020. Production of tapioca starch nanoparticles by nanoprecipitation-sonication treatment. Int. J. Biol. Macromol. 143, 136–142.

Hennia, A., Nemmiche, S., Dandlen, S., Miguel, M.G., 2019. Myrtus communis essential oils: insecticidal, antioxidant and antimicrobial activities: a review. J. Essent. Oil Res. 31, 487–545.

Honarvar Nazari, M., Shihab, M.S., Cao, L., Havens, E.A., Shi, X., 2017. A peony-leaves-derived liquid corrosion inhibitor: protecting carbon steel from NaCl. Green Chem. Lett. Rev. 10, 359–379.

Hong, S., Chen, W., Zhang, Y., Luo, H.Q., Li, M., Li, N.B., 2013. Investigation of the inhibition effect of trithiocyanuric acid on corrosion of copper in 3.0 wt.% NaCl. Corros. Sci. 66, 308–314.

Houbairi, S., Souad, R., Lamiri, A., Essahli, M., 2015. Study of the inhibitory activity of the essential oil of Myrtus communis against copper corrosion in a nitric acid medium.

Huang, H., Guo, X., Bu, F., Huang, G., 2020. Corrosion behavior of immersion silver printed circuit board copper under a thin electrolyte layer. Eng. Fail. Anal. 117, 104807.

Idouhli, R., Oukhrib, A., Koumya, Y., Abouelfida, A., Benyaich, A., Benharref, A., 2018. Inhibitory effect of Atlas cedar essential oil on the corrosion of steel in 1 m HCl. Corros. Rev. 36, 373–384.

Jamshidi, R., Afzali, Z., Afzali, D., 2009. Chemical composition of hydrodistillation essential oil of rosemary in different origins in Iran and comparison with other countries. Am.-Eurasian J. Agric. Environ. Sci. 5, 78–81.

Jerkovic, I., Radonic, A., Borcic, I., 2002. Comparative study of leaf, fruit and flower essential oils of Croatian Myrtus communis (L.) during a one-year vegetative cycle. J. Essent. Oil Res. 14, 266–270.

Jmiai, A., El Ibrahimi, B., Tara, A., Chadili, M., El Issami, S., Jbara, O., Khallaayoun, A., Bazzi, L., 2018. Application of Zizyphus Lotuse-pulp of Jujube extract as green and promising corrosion inhibitor for copper in acidic medium. J. Mol. Liq. 268, 102–113.

Kaco, H., Talib, N.A.A., Zakaria, S., Jaafar, S.N.S., Othman, N.K., Chia, C.H., Gan, S., 2018. ENHANCED CORROSION INHIBITION USING PURIFIED TANNIN IN HCl MEDIUM. Malaysian J. Analyt. Sci. 22, 931–942.

Karthik, N., Lee, Y.R., Sethuraman, M.G., 2017. Hybrid sol-gel/thiourea binary coating for the mitigation of copper corrosion in neutral medium. Prog. Org. Coat. 102, 259–267.

Khaled, K.F., 2010. Corrosion control of copper in nitric acid solutions using some amino acids–A combined experimental and theoretical study. Corros. Sci. 52, 3225–3234.

Khaled, K.F., 2009. Experimental and atomistic simulation studies of corrosion inhibition of copper by a new benzotriazole derivative in acid medium. Electrochim. Acta 54, 4345–4352.

Khaled, K.F., 2008. Molecular simulation, quantum chemical calculations and electrochemical studies for inhibition of mild steel by triazoles. Electrochim. Acta 53, 3484–3492.

Koukos, P.K., Papadopoulou, K.I., Papagiannopoulos, A.D., Patiaka, D.T., 2001. Chemicals from Greek forestry Biomass: Constituents of the leaf Oil of Myrtus communis L. Grown in Greece. J. Essent. Oil Res. 13, 245–246.

Li, C., Guo, X., Shen, S., Song, P., Xu, T., Wen, Y., Yang, H.-F., 2014. Adsorption and corrosion inhibition of phytic acid calcium on the copper surface in 3 wt% NaCl solution. Corros. Sci. 83, 147–154.

Liao, X., Cao, F., Zheng, L., Liu, W., Chen, A., Zhang, J., Cao, C., 2011. Corrosion behaviour of copper under chloride-containing thin electrolyte layer. Corros. Sci. 53, 3289–3298.

López, D.A., Rosero-Navarro, N.C., Ballarre, J., Durán, A., Aparicio, M., Ceré, S., 2008. Multilayer silica-methacrylate hybrid coatings prepared by sol–gel on stainless steel 316L: Electrochemical evaluation. Surf. Coat. Technol. 202, 2194–2201.

Loto, C.A., Akinyele, M., 2020. Effect of ginger, pomegranate and celery extracts on zinc electrodeposition, surface morphology and corrosion inhibition of mild steel. Alexandria Eng. J. 59, 933–941.

Masmoudi, M., Abdelmouleh, M., Abdelhedi, R., 2014. Infrared characterization and electrochemical study of γ-methacryloxypropyltrimethoxysilane grafted in to surface of copper. Spectrochim. Acta Part A Mol. Biomol. Spectrosc. 118, 643–650.

Masmoudi, M., Rahal, C., Abdelhedi, R., Khitouni, M., Bouaziz, M., 2015. Inhibitive action of stored olive mill wastewater (OMW) on the corrosion of copper in a NaCl solution. RSC Adv. 5, 101768–101775.

Messaoud, C., Zaouali, Y., Salah, A.B., Khoudja, M.L., Boussaid, M., 2005. Myrtus communis in Tunisia: variability of the essential oil composition in natural populations. Flavour Fragrance J. 20, 577–582.

Mzioud, K., Habsaoui, A., Ouakki, M., Galai, M., El Fartah, S., Touhami, M.E., 2020. Inhibition of copper corrosion by the essential oil of Allium sativum in 0.5 MH 2 SO 4 solutions. SN Appl. Sci. 2, 1–13.

Nik, W.W., Sulaiman, O., Fadhli, A., Rosliza, R., 2010. Corrosion behaviour of aluminum alloy in seawater, in: Proceedings of MARTEC 2010. The International Conference on Marine Technology. pp. 175–180.

Oyewole, O.A., Mitchell, J., Thresh, S., Zinkevich, V., 2020. The purification and functional study of new compounds produced by Escherichia coli that influence the growth of sulfate reducing bacteria. Egyptian J. Basic Appl. Sci. 7, 82–99.

Özek, T., Demirci, B., Baser, K.H.C., 2000. Chemical composition of Turkish myrtle oil. J. Essent. Oil Res. 12, 541–544.

Pareek, S., Jain, D., Hussain, S., Biswas, A., Shrivastava, R., Parida, S. K., Kisan, H.K., Lgaz, H., Chung, I.-M., Behera, D., 2019. A new insight into corrosion inhibition mechanism of copper in aerated 3.5 wt.% NaCl solution by eco-friendly Imidazopyrimidine Dye: experimental and theoretical approach. Chem. Eng. J. 358, 725–742.

Pereira, P.S., Maia, A.J., Tintino, S.R., Oliveira-Tintino, C.D. de M., Raulino, I.S. de S., Vega, M.C., Rolón, M., Coronel, C., Barros, L. M., Duarte, A.E., 2017. Trypanocide, antileishmania and cytotoxic activities of the essential oil from Rosmarinus officinalis L in vitro. Industrial Crops and Products 109, 724–729.

Perez-Alonso, M.J., Velasco-Negueruela, A., Duru, M.E., Harmandar, M., Esteban, J.L., 1995. Composition of the essential oils of Ocimum basilicum var. glabratum and Rosmarinus officinalis from Turkey. J. Essent. Oil Res. 7, 73–75.

Pino, J.A., Estarrón, M., Fuentes, V., 1998. Essential oil of rosemary (Rosmarinus officinalis L.) from Cuba. J. Essent. Oil Res. 10, 111–112.

Popoola, L.T., 2019. Progress on pharmaceutical drugs, plant extracts and ionic liquids as corrosion inhibitors. Heliyon 5, e01143.

Rahal, C., Masmoudi, M., Abdelhedi, R., Sabot, R., Jeannin, M., Bouaziz, M., Refait, P., 2016. Olive leaf extract as natural corrosion inhibitor for pure copper in 0.5 M NaCl solution: A study by voltammetry around OCP. J. Electroanal. Chem. 769, 53–61.

Refait, P., Rahal, C., Masmoudi, M., 2020. Corrosion inhibition of copper in 0.5 M NaCl solutions by aqueous and hydrolysis acid extracts of olive leaf. J. Electroanal. Chem. 859, 113834.

Rekkab, S., Zarrok, H., Salghi, R., Zarrouk, A., Bazzi, L., Hammouti, B., Kabouche, Z., Touzani, R., Zougagh, M., 2012. Green corrosion inhibitor from essential oil of Eucalyptus globulus (Myrtaceae) for C38 steel in sulfuric acid solution. J. Mater. Environ. Sci 3, 613–627.

Rudresh, H.B., Mayanna, S.M., 1977. Adsorption of n-Decylamine on Zinc from Acidic Chloride Solution. J. Electrochem. Soc. 124, 340.

Shalabi, K., El-Gammal, O.A., Abdallah, Y.M., 2020. Adsorption and inhibition effect of tetraaza-tetradentate macrocycle ligand and its Ni (II), Cu (II) complexes on the corrosion of Cu10Ni alloy in 3.5% NaCl solutions. Colloids Surf., A 609, 125653.

Sharma, Y., Schaefer, J., Streicher, C., Stimson, J., Fagan, J., 2020. Qualitative Analysis of Essential Oil from French and Italian Varieties of Rosemary (Rosmarinus officinalis L.) Grown in the Midwestern United States. Analyt. Chem. Lett. 10, 104–112.

Sherif, E.M., 2012. Inhibition of copper corrosion reactions in neutral and acidic chloride solutions by 5-ethyl-1, 3, 4-thiadiazol-2-amine as a corrosion inhibitor. Int. J. Electrochem. Sci. 7, 2832–2845.

Solmaz, R., 2014. Investigation of corrosion inhibition mechanism and stability of Vitamin B1 on mild steel in 0.5 M HCl solution. Corros. Sci. 81, 75–84.

Stramarkou, M., Oikonomopoulou, V., Missirli, T., Thanassoulia, I., Krokida, M., 2020. Encapsulation of Rosemary Essential Oil into Biodegradable Polymers for Application in Crop Management. J. Polym. Environ.

Szymanska-Chargot, M., Zdunek, A., 2013. Use of FT-IR spectra and PCA to the bulk characterization of cell wall residues of fruits and vegetables along a fraction process. Food Biophys. 8, 29–42.

Tuberoso, C.I., Barra, A., Angioni, A., Sarritzu, E., Pirisi, F.M., 2006. Chemical composition of volatiles in Sardinian myrtle (Myrtus communis L.) alcoholic extracts and essential oils. J. Agric. Food. Chem. 54, 1420–1426.

Wang, L.-H., Sung, W.-C., 2011. Rapid evaluation and quantitative analysis of eugenol derivatives in essential oils and cosmetic formulations on human skin using attenuated total reflectance–infrared spectroscopy. Spectroscopy 26, 43–52.

Zaouali, Y., Messaoud, C., Salah, A.B., Boussaid, M., 2005. Oil composition variability among populations in relationship with their ecological areas in Tunisian Rosmarinus officinalis L. Flavour Fragrance J. 20, 512–520.

Zhang, Z., Cui, J., Zhang, J., Liu, D., Yu, Z., Guo, D., 2019. Environment friendly chemical mechanical polishing of copper. Appl. Surf. Sci. 467, 5–11.

Znini, M., Majidi, L., Bouyanzer, A., Paolini, J., Desjobert, J.-M., Costa, J., Hammouti, B., 2012. Essential oil of Salvia aucheri mesatlantica as a green inhibitor for the corrosion of steel in 0.5 M H2SO4. Arabian J. Chem. 5, 467–474.